

## Chapter 2

### Experimental Setup and Overview

#### 2.1 Experimental Apparatus and techniques

In most of the experiments in this thesis, a three step excitation scheme is used to produce a time dependent photoionization signal, and hence observe time dependent wave packet dynamics as presented in the previous chapter. The experimental setup uses a cw launch state preparation laser to excite the transition for  $A^1\Sigma_u^+ \leftarrow X^1\Sigma_g^+$ , an ultrafast laser system to produce the pump and variably delayed probe pulses, a pulse shaping apparatus, a heat pipe containing the  $\text{Li}_2$  sample, various detection apparatuses, and controlling software on a computer.

The laser system is pumped by an argon ion ( $\text{Ar}^+$ ) laser operating at  $\sim 27$  W, which pumps a cw dye laser for launch state preparation, and various ultrafast lasers, depending upon the experiment [see Fig. 2.1 for a sample excitation scheme]. The experimental laser setup will be discussed in more detail in the respective section where data will be presented, since the setup changes depending upon the experiment. Figure 2.2 summarizes the optical table layout, with notes where the laser setup is changed. In almost all cases, three lasers interact to produce photoions, and pump-probe experiments are performed. It is duly noted where the excitation scheme deviates from a three laser interaction.

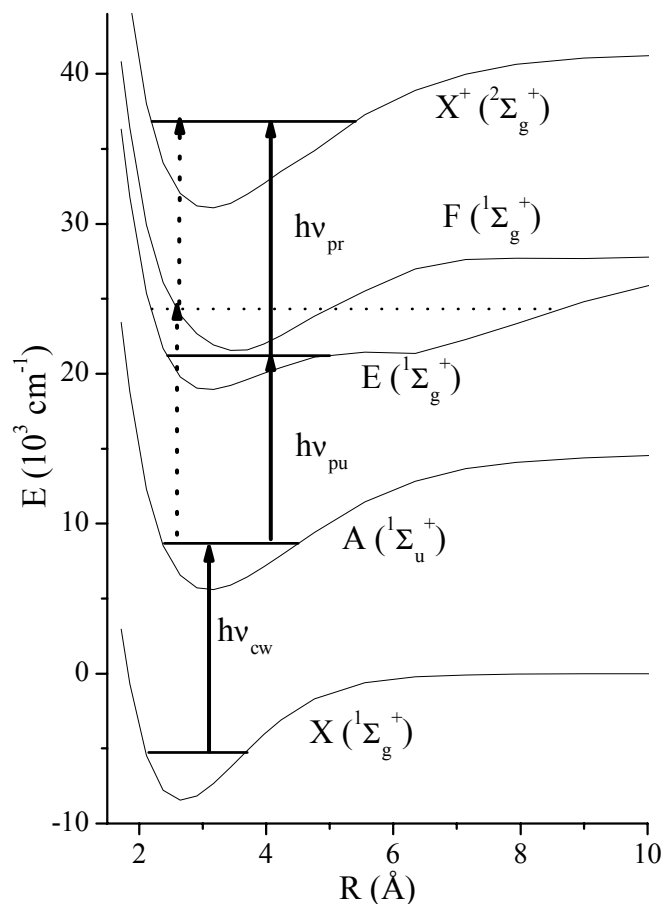


Figure 2.1: Typically excited potential energy curves in  $\text{Li}_2$ . In this scheme, the pump and probe pulses are of different colors. A cw laser excites from the  $X (^1\Sigma_g^+)$  electronic curve to a pure launch state on  $A (^1\Sigma_u^+)$ . An 800 nm ultrafast laser excites a superposition of states on the  $E (^1\Sigma_g^+)$  curve, which is subsequently ionized by a time delayed 640 nm ultrafast probe pulse. At negative delays (dotted lines), the probe-pump pathway (for 640 nm probe pulse) through the  $F (^1\Sigma_g^+)$  state, as indicated by the dotted lines, has a much lower yield than the positive time pathway due to unfavorable Frank-Condon overlap factors. Note that in some experiments, as described in the appropriate chapters, the excitation scheme will deviate from above.

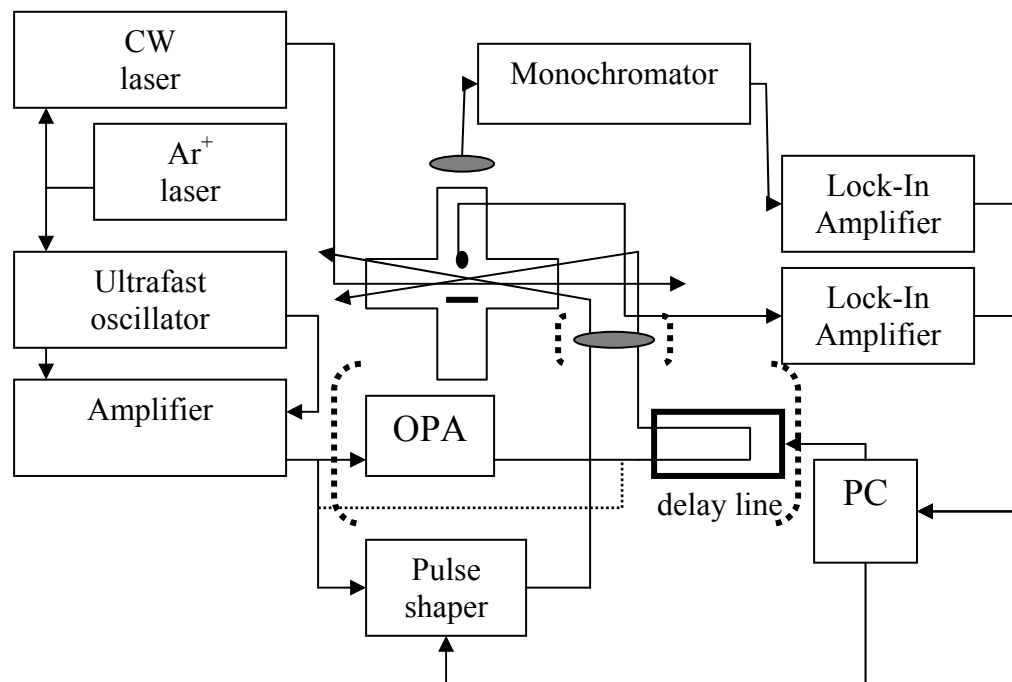


Figure 2.2: Schematic experimental setup. Sections in parentheses indicate changeable portions of the setup. The output from the regenerative amplifier is divided into up to two beams. One beam goes through the pulse shaper. This beam can be either the pump or probe pulse, depending on the pulse timing, but is actively shaped only in experiments where it is acting as the pump pulse. The second beam is either split unchanged or goes through the OPA to produce tunable ultrafast output from 500-700 nm. The ultrafast and cw beams intersect in the heat pipe which is equipped to detect ions and fluorescence. Focusing optics can be placed into the beam lines to increase peak intensity.

### 2.1.1 Pulse shaper

Since many of the experiments described in this thesis depend exquisitely on the manipulation of ultrafast dynamics by phase and amplitude shaping the spectrum of an ultrafast laser pulse, it is necessary to discuss the pulse shaping setup in some detail. The pulse shaper consists of a zero dispersion, four focal length imaging system, and uses a spatially addressable, double stack 128 pixel SLM between crossed polarizers, in a setup similar to that described by Weiner *et al.*[30] and Wefers *et al.*[29, 34, 35] In the Fourier plane, the pulse is dispersed linearly with respect to wavelength across the face of the SLM. Generally, the bandwidth of our pulses is dispersed across up to 40 pixels (FWHM) on the SLM. With a pulse bandwidth of 9 nm, this results in approximately  $4 \text{ cm}^{-1}$  per pixel resolution for frequency domain pulse shaping. By applying specific voltages to the pixels, we can manipulate the phase and amplitude of each wavelength of the pulse.

With a single frequency imaged to a spot size of  $170 \text{ }\mu\text{m}$ , the broadband pulses can be temporally shaped within a time envelope approximately 8 ps wide (referred to as the “pulse shaping window”), as derived previously [29] and observed experimentally. This envelope, which will be an important experimental constraint, is a result of both the sampling effects of the finitely sized pixels of the SLM and the finite spot size for each frequency component. To shift a pulse in time, a linear phase is applied across the pulse according to  $\Delta t = d\phi/d\omega$ . The sampling aspect of the SLM gives an approximation to this formula to be

$\Delta t = \Delta\phi / \Delta\omega_{pix}$  where  $\Delta\phi$  is the phase shift per pixel, and  $\Delta\omega_{pix}$  is the difference in central frequencies imaged onto adjacent pixels. Because of wrap around of phases, a phase shift of  $\Delta\phi$  can also be represented as  $\Delta\phi + 2n\pi$ , where  $n$  is an integer. This produces replicas at  $\Delta t = (\Delta\phi + 2n\pi) / \Delta\omega_{pix}$  and attenuates the shifted pulses with attenuation increasing along with  $\Delta t$ . Another limitation is the finite spot size: spatial overlap of more than one pixel by a monochromatic wavelength causes diffraction of certain wavelengths out of the beam. This is because the  $\Delta\phi$  between adjacent pixels introduces a certain amount of destructive interference. We thus see some destructive interference in the direction of propagation, as light that is produced with the multiple phases is diffracted out of the beam to maintain momentum matching conditions[29].

In many of the experiments here, we shape the pump pulse, and the electric field can be written as

$$E(t) = \sum_{i=1}^{128} \int_{-\infty}^{\infty} d\omega_i' | \varepsilon_i(\omega_i') | T_i'^{1/2} \exp[i(\omega_i' t + \phi_i)], \quad (2.1)$$

where the summation is over all 128 pixels across the SLM, and  $\varepsilon(\omega_i')$  is the amplitude of the electric field at the central frequency  $\omega_i'$  on each pixel. The amplitude and phase controls over the pulse are included in the  $T_i'^{1/2}$  and  $\phi_i$  terms, which represent the absolute value of the amplitude transmittance and applied phase, respectively. Without modulation,  $T_i'^{1/2} = 1$ , and  $\phi_i = 0$ . The  $\varepsilon_i(\omega_i')$  term is approximately Gaussian, to reflect the spectrum imaged onto a single pixel, and it will be shown that this bandwidth is approximately  $6 \text{ cm}^{-1}$ , as opposed to the separation of central frequencies on adjacent pixels of  $4 \text{ cm}^{-1}$ . Note that the

integrals of adjacent pixels will have significant overlap, resulting in attenuation of the field when phase shifts between adjacent pixels are applied. In typical experiments, excitation is in the weak field, but some experiments will examine stronger field effects. In the experiments described in this thesis, peak electric fields range from  $10^5$ - $10^{11}$  W/cm<sup>2</sup>, depending upon the experiment.

As an experimental demonstration of the capabilities of the pulse shaping apparatus, a series of phase locked pulses was generated. First, Fig. 2.3 shows the extent to which a phase locked pulse train can be created with our pulse shaping setup. It is evident from the figure that longer time delays between pulses means less intense pulses, as expected from the diffraction effect argument from above. The longest time delay between pulses of about 8.5 ps demonstrates a limit of pulseshaping. Notice that as the pulse separation increases, the pulse intensity decreases; diffraction due to phase shifts of adjacent pixels decreases the transmitted intensity of phase shaped pulses. In a phase locked pulse replica scheme, a phase grating with an alternation between 0 and  $\pi$  phase between adjacent pixels is applied to the SLM. This represents the maximum linear phase that can be applied. Any more than a  $\pi$  phase shift between adjacent pixels, because of wrap-around effect, will be equivalent to a smaller phase shift with the opposite sign. In later chapters, several instances of pulse-shaping will be cited, and the decrease in pulse intensity seen above will become important.

A second example of a pulse-shaping scheme can be useful for illustrating the limitations of our pulse shaper. Figure 2.4 shows a two-color pulse train,

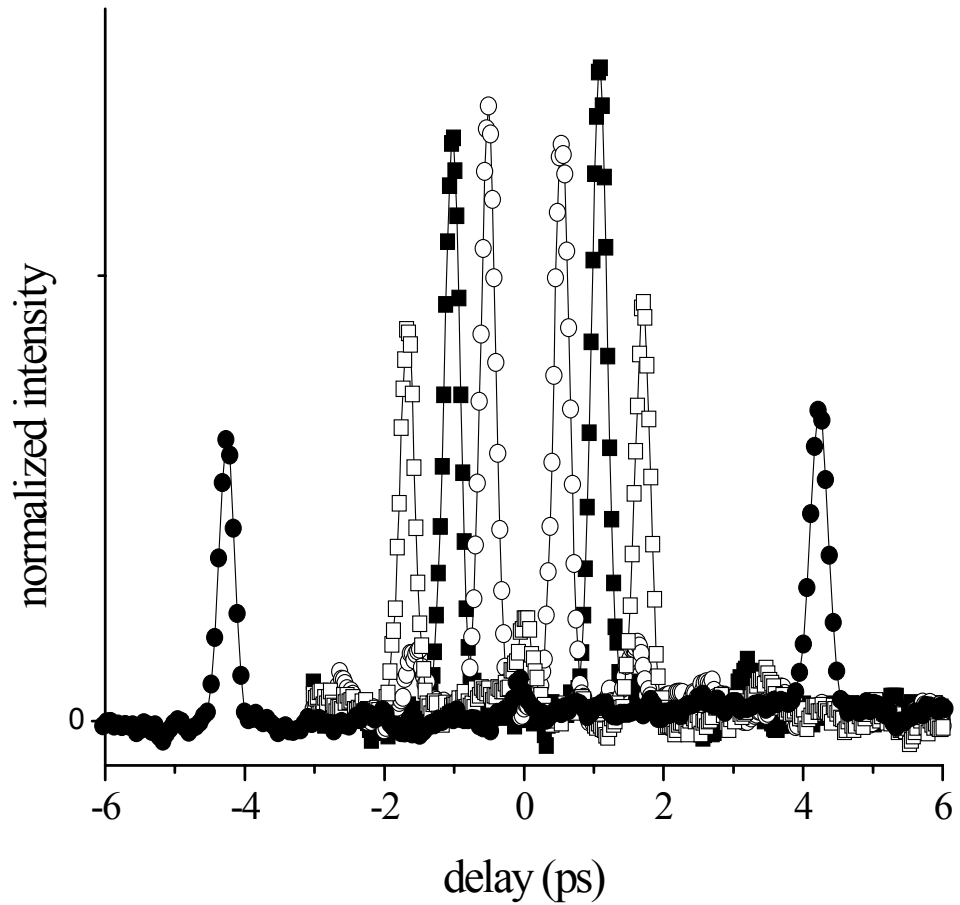


Figure 2.3: Cross correlation pulse profiles for pulse trains with various interpulse delays. The pulse trains are generated by the application of a phase grating of  $\pi \cdot \text{round}[\cos^2(2\pi p)]$ , where *round* indicates rounding to the nearest integer (0 or 1), and *p* indicates a number of pixels from 2 to 16, for the longest to shortest interpulse delay, respectively. The symbols represent scans for different delays between phase locked pulses.

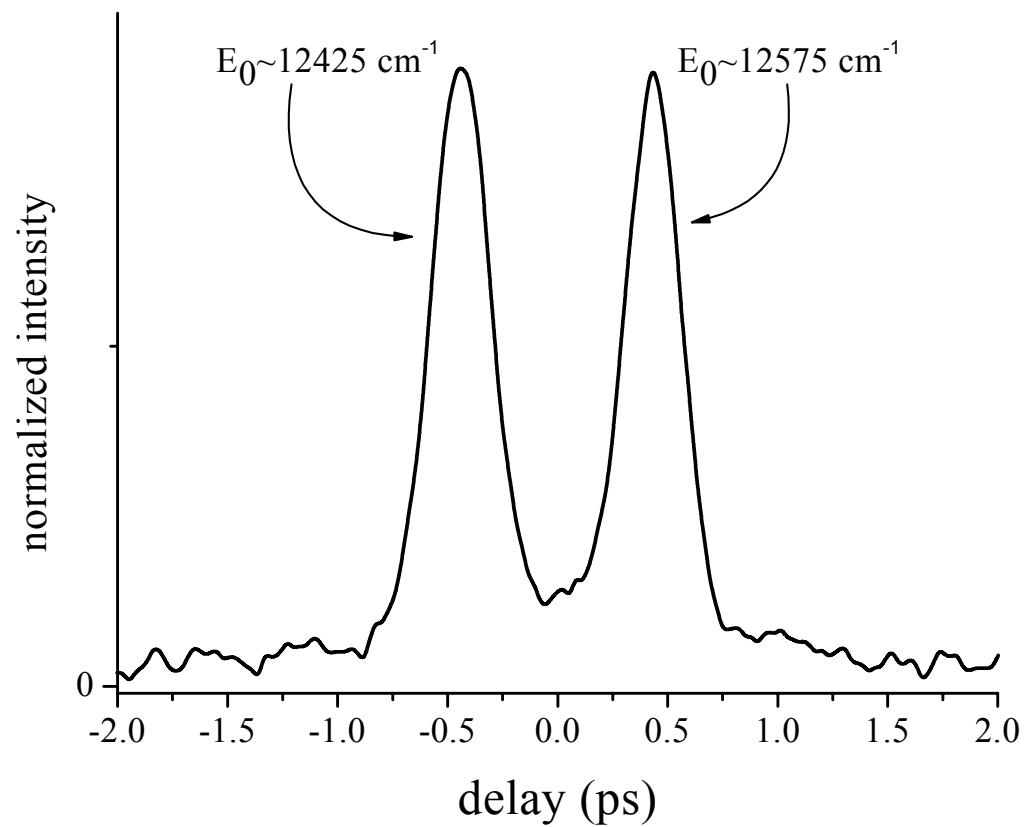


Figure 2.4: Multi-color pulse train. The pulse train was generated by applying opposing linear phases to the high ( $E > E_{i0}$ ) and low energy ( $E < E_{i0}$ ) halves of the input spectrum centered at  $E_{i0}$ .

where two phase related pulses are generated that each correspond to a different half of the input spectrum. The pulse train is generated by applying a linear phase  $\varphi(p) = \pm mp$  where  $p$  is the pixel number and  $m$  is a constant. All wavelengths with a shorter than average wavelength get a positive slope to the phase, and those with a longer than average wavelength get a negative slope. The net effect of this is to create two pulses that are equally spaced around  $t=0$  and have pulse durations approximately twice as long as transform-limited pulses. This pulse train is demonstrated here because of its potential importance in strong field control schemes such as stimulated Raman adiabatic passage (STIRAP)[36].

### **2.1.2 Heat pipe/detection**

The lithium dimer sample is contained in a static heat pipe, which is operated at 750°-800° C, with an argon buffer gas pressure of between 1.0 and 3.5 Torr, depending upon the experiment. The lithium atom pressure at this temperature is approximately 1 Torr (130 Pa), which will give a  $\text{Li}_2$  pressure of approximately 0.02 Torr (2.6 Pa). The lasers intersect between two parallel plate electrodes that are separated by 1 cm with 10 V applied across them. The current generated by the ionization of the molecules is measured by a lock-in amplifier, which is synchronized to the modulation of the cw laser at 750 Hz by a mechanical chopper. This technique gives a maximum single scan signal-to-noise ratio of up to 10:1.

Signals are generally normalized to the fluorescence from the launch state. This is accomplished by observing fluorescence in a perpendicular geometry [see

Fig. 2.2]. All fluorescent light within the small solid angle bounded by a 2" collection lens is imaged onto a fiber-optic bundle. This fiber bundle then couples into a monochromator, and the light for a specific transition [e. g. A(11, 28)→X(2, 29)] is detected with a photomultiplier tube driven at 950 V. The output voltage is then filtered with a lock-in amplifier, and the photoionization is divided by the fluorescence in real time. The net effect of this is that drift in the power or wavelength of the cw laser becomes less important.

## 2.2 Wavelength Subtraction Spectroscopy

One of the main traits of ultrafast lasers that separates them from other pulsed or continuous wave (cw) lasers is the wide spectral bandwidth inherent due to the Heisenberg Uncertainty Principle. Since the ultrafast lasers occur on such a short timescale, they are characterized by a wide spectral bandwidth. In studying any sort of ultrafast transition, this wide bandwidth can affect the dynamics of the transition. CW absorption spectroscopy can to a certain extent give complete information describing a transition, but interactions between wavelengths can be lost. As an alternative, Wavelength Subtraction Spectroscopy (WSS), where a transition is measured with a spectral notch in the excitation spectrum, can be used to look at the relationship of different frequencies in an excitation by an ultrafast pulse. This becomes especially important in examining either strong field or phase shaped pulses.

To study the effects of the wide bandwidth on a transition, there are several methods one can use. The first, and perhaps most obvious, is to perform a

variant of tunable cw absorption spectroscopy, where a laser is tuned and absorption is measured, giving an absorption linewidth, followed by performing an Inverse Fourier Transform to infer the time dynamics. In this regime, the signal will simply be a summation of the single frequency components in the signal:

$$S = \left| \int d\omega A(\omega) \right|^2 \quad (2.2)$$

where  $A(\omega)$  is simply the signal amplitude—such as an excited state coefficient—expected for any single exciting wavelength; time dependence is implied. For the case of a two state wave packet, it can easily be inferred that the two states interact if coherently excited, so that  $S = |A(\omega_1) + A(\omega_2)|^2$ , but as an excitation gets more complex, making inferences such as this get more and more complex, as well.

In contrast, WSS can give direct information about the nature of an excitation. As implemented in our experiments, one pixel at a time is blocked on the SLM, as shown in Fig. 2.5. For each gathered data point, the signal is characterized by the following:

$$S_{WSS}(\omega') \propto \left| \int_{\omega} d\omega A(\omega) - \int_{\omega'} d\omega' A(\omega') \right|^2 \quad (2.3)$$

where the integration over  $\omega$  is the base spectrum, the integration over  $\omega'$  is the subtracted part of the spectrum, and again  $A(\omega)$  is a frequency dependent amplitude with the time dependence implied. The crucial difference between this spectrum and what one would expect from a cw type experiment is that there are now cross terms between the frequency components  $\omega'$  and  $\omega$ :

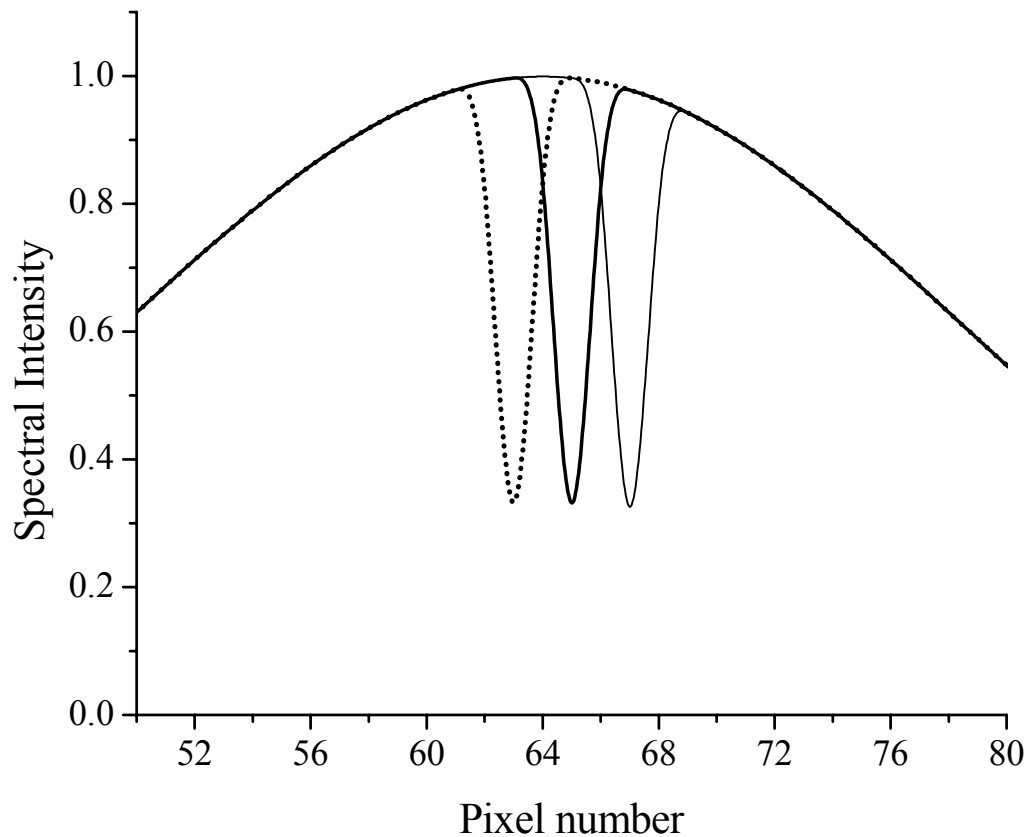


Figure 2.5: Schematic spectra as used in Wavelength Subtraction Spectroscopy (WSS). A signal is acquired for each spectrum as one single pixel at a time is blocked. In the experiment, the light on each pixel is completely attenuated, but when the SLM mask is converted to wavelength units, a single frequency is not completely attenuated due to focusing effects. Three wavelength spectra are shown in the figure as pixels 63, 65, and 67 are sequentially blocked.

$$S_{WSS}(\omega') \propto \int_{-\infty}^{\infty} d\omega |A(\omega)|^2 + \int_{-\infty}^{\infty} d\omega' |A(\omega')|^2 - \int_{-\infty}^{\infty} \int_{-\infty}^{\infty} d\omega d\omega' [A^*(\omega)A(\omega') + A^*(\omega')A(\omega)]. \quad (2.3b)$$

In a case where there is only one resonance present, and the field is weak, the cross terms are significant only when  $\omega$  and  $\omega'$  are resonant frequencies[7]. In the two resonance case mentioned above, the only cross term is where  $\omega$  and  $\omega'$  represent the two resonant frequencies, and it only modulates the depth of the signals. In more complex cases, the cross terms can become numerous, drastically changing depth and width of the observed signal. New information, including the amplitude of an excitation relative to all other excitation pathways, can now be extracted from a simple spectrum. Since, in pulse shaping schemes, interferences between spectral pathways are often invoked to manipulate a system, this technique gives a measure of the interference (see chapter 5).

To illustrate, Fig. 2.6 shows a comparison of the two cases for examining an excitation at a specific time during an excitation of a two level system. In both cases, the same phase mask is applied to the SLM. In one case, it is assumed that the SLM *transmits* the light from only one pixel at a time, and in the second case, it is assumed that the SLM *attenuates* the light on one pixel at a time. A perturbative calculation is then performed to find an excited state population at a transient time (details of the calculation procedures are presented in chapter 6). The main result to be considered here is that the two types of spectroscopies present qualitatively different results under certain conditions. WSS is basically a type of optical heterodyne detection. In WSS, phase information is gleaned from the signal since the data is gathered with a certain coherent background, as

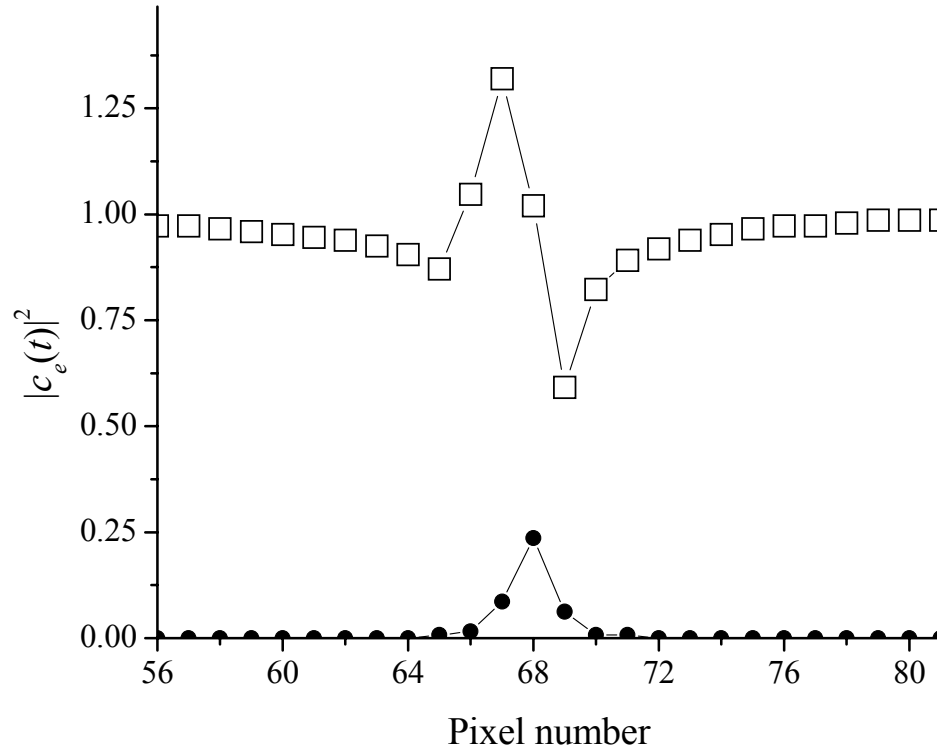


Figure 2.6: Comparison of excited state populations for a weak, phase shaped input using narrow bandwidth excitation and WSS. The dots (●) represent the calculated excited state population at  $t=0.0$  ps with an excitation laser bandwidth equal to the spectrum imaged onto a single pixel of an SLM, scanned pixel by pixel. The squares (□) represent the calculated excited state population at  $t=0.0$  ps using the WSS method. In both cases, an identical phase mask is used.

represented by all other frequencies in the full pulse. In following chapters, the WSS spectroscopic technique will be used in both the limited-cross-term regime and the highly coupled regime.